The luminous type Ia supernova 2022ilv and its early excess emission

Srivastav, S., Smartt, S. J., Huber, M. E., Dimitriadis, G., Chambers, K. C., Fulton, M. D., Moore, T., Callan, F. P., Gillanders, J. H., Maguire, K., Nicholl, M., Shingles, L. J., Sim, S. A., Smith, K. W., Anderson, J. P., de Boer, T., Chen, T.-W., Gao, H., & Young, D. R. (2023). The luminous type Ia supernova 2022ilv and its early excess emission. *The Astrophysical Journal Letters*, *943*(2), Article L20. https://doi.org/10.3847/2041-8213/acb2ce

Document Version:
Publisher's PDF, also known as Version of record

Queen's University Belfast - Research Portal:
Link to publication record in Queen's University Belfast Research Portal

The Luminous Type Ia Supernova 2022ilv and Its Early Excess Emission

Shubham Srivastav[1], S. J. Smartt[1,2], M. E. Huber[3], G. Dimitriadis[4], K. C. Chambers[3], Michael D. Fulton[1], Thomas Moore[1], F. P. Callan[1], James H. Gillanders[5], K. Maguire[4], M. Nicholl[6], Luke J. Shingles[1,7], S. A. Sim[1], K. W. Smith[1], J. P. Anderson[8,9], Thomas de Boer[3], Ting-Wan Chen[10,11], Hua Gao[3], and D. R. Young[1]

[1] Astrophysics Research Centre, School of Mathematics and Physics, Queen's University Belfast, Belfast BT7 1NN, UK; s.srivastav@qub.ac.uk
[2] Department of Physics, University of Oxford, Keble Road, Oxford OX1 3RH, UK
[3] Institute for Astronomy, University of Hawaii, 2680 Woodlawn Drive, Honolulu, HI 96822, USA
[4] School of Physics, Trinity College Dublin, The University of Dublin, Dublin 2, Ireland
[5] Department of Physics, University of Rome "Tor Vergata," Via della Ricerca Scientifica 1, I-00133 Rome, Italy
[6] Birmingham Institute for Gravitational Wave Astronomy and School of Physics and Astronomy, University of Birmingham, Birmingham B15 2TT, UK
[7] GSI Helmholtzzentrum für Schwerionenforschung, Planckstraße 1, D-64291 Darmstadt, Germany
[8] European Southern Observatory, Alonso de Córdova 3107, Casilla 19, Santiago, Chile
[9] Millennium Institute of Astrophysics MAS, Nuncio Monsenor Sotero Sanz 100, Off. 104, Providencia, Santiago, Chile
[10] Technische Universität München, TUM School of Natural Sciences, Physik-Department, James-Franck-Straße 1, D-85748 Garching, Germany
[11] Max-Planck-Institut für Astrophysik, Karl-Schwarzschild Straße 1, D-85748 Garching, Germany

Abstract

We present observations and analysis of the hostless and luminous Type Ia supernova 2022ilv, illustrating it is part of the 2003fg-like family, often referred to as super-Chandrasekhar (Ia-SC) explosions. The Asteroid Terrestrial-impact Last Alert System light curve shows evidence of a short-lived, pulse-like early excess, similar to that detected in another luminous Type Ia supernova (SN 2020hvf). The light curve is broad, and the early spectra are remarkably similar to those of SN 2009dc. Adopting a redshift of $z = 0.026 \pm 0.005$ for SN 2022ilv based on spectral matching, our model light curve requires a large ^{56}Ni mass in the range 0.7–1.5 $M_\odot$ and a large ejecta mass in the range 1.6–2.3 $M_\odot$. The early excess can be explained by fast-moving SN ejecta interacting with a thin, dense shell of circumstellar material close to the progenitor ($\sim 10^{13}$ cm) a few hours after the explosion. This may be realized in a double-degenerate scenario, wherein a white dwarf merger is preceded by the ejection of a small amount ($\sim 10^{-3}$–10^{-2} $M_\odot$) of hydrogen and helium-poor tidally stripped material. A deep pre-explosion Pan-STARRS1 stack indicates no host galaxy to a limiting magnitude of $r \sim 24.5$. This implies a surprisingly faint limit for any host of $M_r \gtrsim -11$, providing further evidence that these types of explosions occur predominantly in low-metallicity environments.

Unified Astronomy Thesaurus concepts: Supernovae (1668); Type Ia supernovae (1728)

Supporting material: machine-readable table

1. Introduction

A rare subclass of Type Ia supernovae (SNe Ia) is often referred to as "super-Chandrasekhar" Ia or Ia-SC. The observational properties of this subclass are defined by the prototype SN 2003fg (Howell et al. 2006) along with SNe 2006gz, 2007if, and 2009dc (Hicken et al. 2007; Scalzo et al. 2010; Taubenberger et al. 2011), among others. Their broad light curves would require $\gtrsim 1\ M_\odot$ of radioactive ^{56}Ni and well over a Chandrasekhar mass ($M_{\rm Ch}$) of ejecta. However, we now understand that this is a diverse subclass of objects (Ashall et al. 2021), with peak luminosities ranging from $M_B^{\rm peak} \approx -19.1$ for ASASSN-15hy (Lu et al. 2021) to $M_B^{\rm peak} \approx -20.4$ for SN 2006gz and SN 2009dc (Scalzo et al. 2010; Taubenberger et al. 2011).

The subclass is generally characterized by high luminosities, broad light curves, relatively low expansion velocities, and high ultraviolet (UV) and near-infrared (NIR) luminosities, posing a challenge for theoretical models (Taubenberger 2017). Most of these events do not follow the width–luminosity relation, typically showing negative Hubble residuals (Ashall et al. 2021).

Early observations a few hours to days past explosion are a vital diagnostic tool for investigating the SN Ia explosion mechanism and nature of the binary companion (Maoz et al. 2014). A significant fraction ($\sim 20\%$) show evidence of a flux excess in their early light curves (Magee et al. 2020; Deckers et al. 2022). Multiple physical mechanisms have been proposed—SN ejecta colliding with a binary companion within the single-degenerate scenario (e.g., Kasen 2010), SN ejecta interacting with extended circumstellar material (e.g., Levanon & Soker 2017), the presence of ^{56}Ni clumps in the outermost layers of the ejecta (e.g., Shappee et al. 2019), and helium shell detonations occurring on the WD surface in the double-detonation scenario (e.g., Polin et al. 2019).

Recently, an early flux excess was detected for the peculiar, luminous Ia SN 2020hvf by Jiang et al. (2021), who invoked circumstellar material (CSM) interaction involving $\sim 10^{-2}\ M_\odot$ of extended material at a distance of $\sim 10^{13}$ cm. A tentative early excess was also reported for ASASSN-15pz (Chen et al. 2019) and LSQ 12gpw (Jiang et al. 2018). It is possible that the early excess is ubiquitous in this subclass, which may help understand their progenitor channel. In this paper, we present another clear discovery of a flux excess in the early light curve

Table 1
Summary of Photometric Observations of SN 2022ilv and SN 2020hvf

SN	MJD	Mag	Error	Instrument	Filter
2022ilv	59689.38	19.36	0.28	ATLAS	o
2022ilv	59690.52	>20.02	⋯	ATLAS	o
2022ilv	59691.26	19.44	0.15	ATLAS	o
2022ilv	59692.48	18.64	0.09	ATLAS	c
2022ilv	59694.49	17.70	0.03	ATLAS	o
2022ilv	59695.21	17.36	0.02	ATLAS	o

Note. All magnitudes are in the AB system.

(This table is available in its entirety in machine-readable form.)

of a luminous Type Ia (SN 2022ilv) with extensive photometric and spectroscopic data and light-curve models.

2. Discovery and Follow-up

SN 2022ilv was discovered by the Zwicky Transient Facility (ZTF; Bellm et al. 2019) on 2022 April 24.30 UT, or MJD 59693.30, at a magnitude of $r = 18.32 \pm 0.07$. It was classified by Burke et al. (2022) on MJD 59698.63 as a super-Chandrasekhar SN Ia (Ia-SC) at a redshift of $z = 0.031$.

We independently flagged it as a "real" transient in the Asteroid Terrestrial-impact Last Alert System (ATLAS; Tonry et al. 2018b) survey data on MJD 59692.48, a day prior to ZTF discovery (Smith et al. 2020). The ATLAS units covered the position of SN 2022ilv on four epochs (each with 4×30 s) between 59689.39 and 59992.48, all before the ZTF discovery (see Section 3.1).

We triggered follow-up photometric and spectroscopic observations of SN 2022ilv at the 2 m Liverpool Telescope (LT; Steele et al. 2004) under programs PL22A20 and PL22B16 (PI Srivastav), and PL22A13 (PI Dimitriadis). Point-spread function (PSF) photometry in $griz$ was calibrated against Pan-STARRS1 (PS1) reference stars and the u band was calibrated using Sloan Digital Sky Survey (SDSS) data. ZTF magnitudes in gr bands were obtained through the Lasair broker[12] (Smith et al. 2019). We also obtained images in the iz bands using the 1.8 m Pan-STARRS2 (PS2) telescope (Chambers et al. 2016). The PS2 data were processed through the Image Processing Pipeline (IPP; Magnier et al. 2020), and image subtraction was performed using PS1 3π survey data (Chambers et al. 2016) as reference.

SN 2022ilv was also observed by the Ultraviolet and Optical Telescope (UVOT; Roming et al. 2005) on Swift (Gehrels et al. 2004). Four epochs of imaging were obtained and photometry was performed using the `uvotsource` task within the High Energy Astrophysics SOFTware (HEASOFT) package, following Brown et al. (2009).

The photometry of SN 2022ilv and SN 2020hvf is summarized in Table 1.

2.1. Search for the Host Galaxy

There is no host galaxy candidate coincident with the SN location visible in the Pan-STARRS1 3π images (Chambers et al. 2016) or the Dark Energy Camera Legacy Survey (DECaLS; Dey et al. 2019) and no galaxies with a cataloged spectroscopic redshift in the NASA Extragalactic Database (NED) within a $4\rlap{.}'5$ radius of SN 2022ilv. We combined 328

---
[12] https://lasair-ztf.lsst.ac.uk/object/ZTF22aahhywm/

pre-explosion Pan-STARRS1 w-band (a broad $g + r + i$ composite filter) exposures, with a total effective exposure of 7800 s, to create a deep reference stack. The stacked image (Figure 1) does not reveal a candidate host galaxy at the location of SN 2022ilv. Assuming $(w - r) \approx 0$, we estimate a 3σ limiting magnitude of $r \gtrsim 24.5$ mag (AB). Depending on the adopted distance (see Section 2.2), the upper limit on the host luminosity is $M_r \gtrsim -11$ to -10.

The two sources with the least angular offset to the SN location are marked in the w-band stack (Figure 1). Source 1, offset by $1\rlap{.}''2$ east and $3\rlap{.}''4$ south of SN 2022ilv, is a red point-like source, a likely foreground star. Source 2, offset by $10\rlap{.}''4$ west and $3\rlap{.}''5$ south, is an extended source and was considered a potential host galaxy candidate. A spectrum of the galaxy, obtained from the Inamori Magellan Areal Camera and Spectrograph (IMACS) instrument on the Magellan telescope on 2022 May 20, reveals emission lines at a redshift $z \approx 0.11$, clearly incompatible with any reasonable classification for SN 2022ilv.

2.2. Redshift and Distance

In the absence of a host galaxy redshift, the redshift was constrained using the spectral template matching tool SNID (Blondin & Tonry 2007). We added the spectra of 2003fg-like events SN 2007if (Scalzo et al. 2010) and SN 2009dc (Taubenberger et al. 2011) to the SNID template library that already contained the spectra of SN 2006gz. The top matches on SNID are consistent with SN 2009dc and SN 2006gz for the premaximum spectra. The spectra of SN 2022ilv show excellent matches with SN 2009dc and SNID favors a low redshift of $z = 0.020$–0.022. For SN 2006gz, SNID favors a higher redshift of $z = 0.030$–0.032. Fits to normal SNe Ia spectra are inferior around the maximum and premaximum epochs, although not unreasonable postmaximum. Normal SN Ia spectra at maximum do not show the prominent and persistent C II feature exhibited by SN 2022ilv, which is a signature of 2003fg-like SNe. The normal SN Ia matches require a redshift of $z = 0.030$–0.035, implying peak absolute magnitudes of $M_g < -20$ for SN 2022ilv, incompatible with normal SNe Ia. Based on the matches with SN 2006gz and SN 2009dc, we adopt a mean redshift of $z = 0.026$, with a range of $0.021 < z < 0.031$. Assuming a flat universe with $\Omega_M = 0.3$ and adopting $H_0 = 70$ km s^{-1} Mpc^{-1} implies a mean luminosity distance of 114 Mpc with a range 91–136 Mpc (distance modulus $\mu = 35.28^{+0.39}_{-0.47}$ mag). For the subsequent analysis, we present the properties of SN 2022ilv at this range of distances.

3. Light Curve and Spectral Data

3.1. Early Flux Excess

We manually performed forced photometry on all the 30 s difference images from ATLAS over the supernova duration and before discovery. This forces a PSF fit that is obtained from the individual input images prior to subtraction at the mean position of the source. The forced photometry flux ($f \pm f_{err}$) is calibrated with stars in RefCat2 (Tonry et al. 2018a) in units of microjansky (μJy). We compute a combined weighted flux (F) from the fluxes (f_i) measured in the quad of exposures on a nightly basis, using weights dependent on the measurement
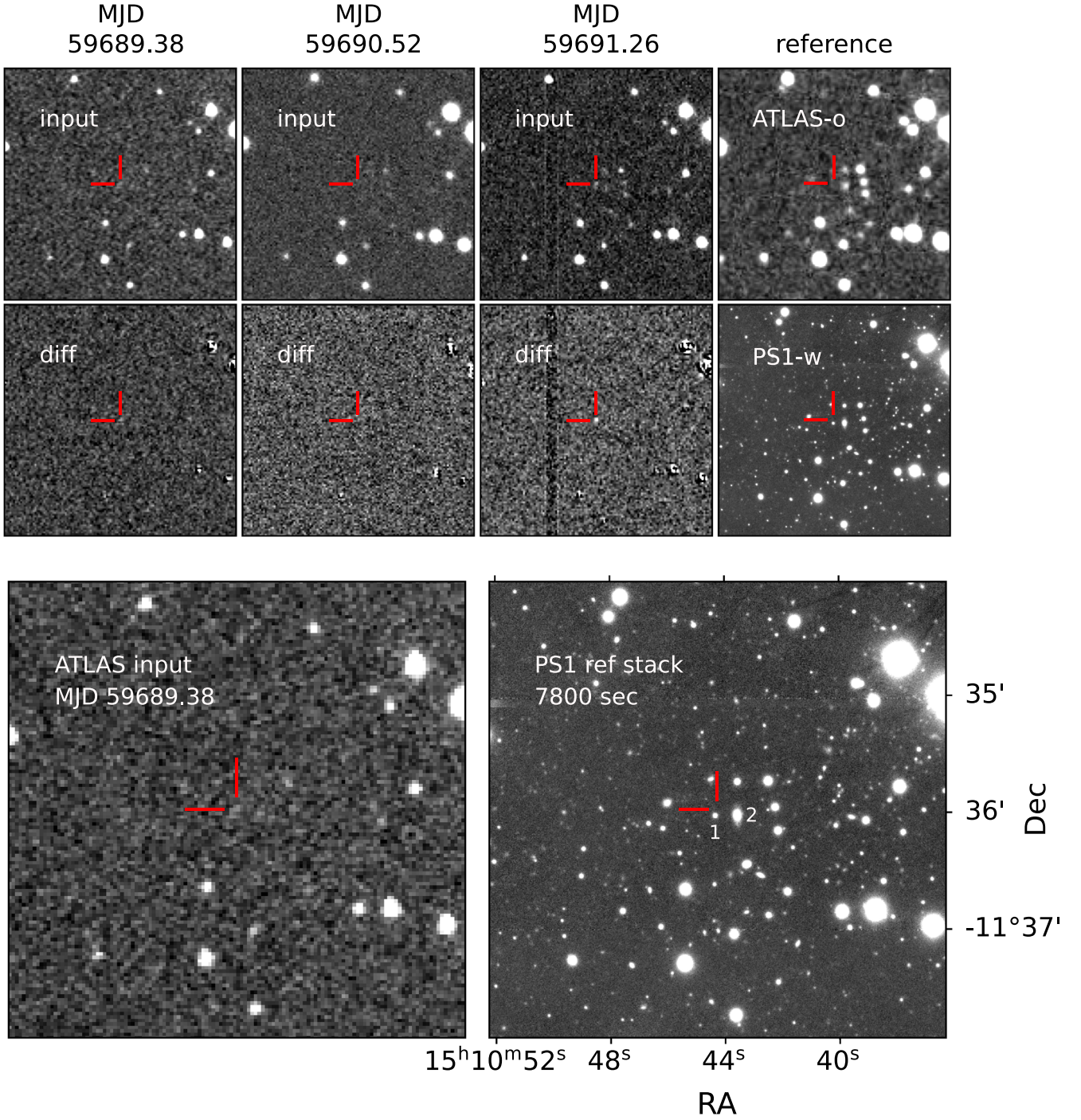
Figure 1. ATLAS and Pan-STARRS1 images for the field of SN 2022ilv. Top row (left to right): median-combined ATLAS input images on MJDs 59689.38, 59690.52, and 59691.26 and the reference ATLAS template used for the subtraction. Middle row: median-combined ATLAS difference images on MJDs 59689.38, 59690.52, and 59691.26 and the deep Pan-STARRS1 w-band stack with an effective exposure time of 7800 s. Bottom row: median-combined ATLAS input image on MJD 59689.38 and the Pan-STARRS1 reference stack. The SN position is marked by the cross-hairs. Two sources closest to the SN position are marked. Source 1 is a foreground star, and source 2 is a galaxy at $z \approx 0.11$, and thus ruled out as a host galaxy candidate for SN 2022ilv.

uncertainties, $w_i = \Delta f_{i,\mathrm{err}}^{-2}$:

$$F = \frac{\sum_i w_i \times f_i}{\sum_i w_i}. \tag{1}$$

This results in a 3.9σ detection on MJD = 59689.38 (median time of the quad) in the o band at $F = 65.7 \pm 16.8\,\mu$Jy or $o = 19.36 \pm 0.28$ mag. The stacked measurements show 5σ detections on MJD 59691.26 and beyond, but we see a nondetection in the intervening epoch of MJD 59690.52, at

$F = 23.3 \pm 11.9\,\mu$Jy, corresponding to a 3σ upper limit of $o > 20.02$). To illustrate the reliability of these combined flux measurements on the individual frames, we also coadded the images. The four individual 30 s exposures on each of the MJD epochs 59689.38, 59690.52, and 59691.26 were aligned and combined with median coaddition (Figure 1). Visual inspection of the coadded input and difference images confirms the presence of residual flux at the SN location on MJD 59689.38, followed by no obvious detection the next day, on MJD
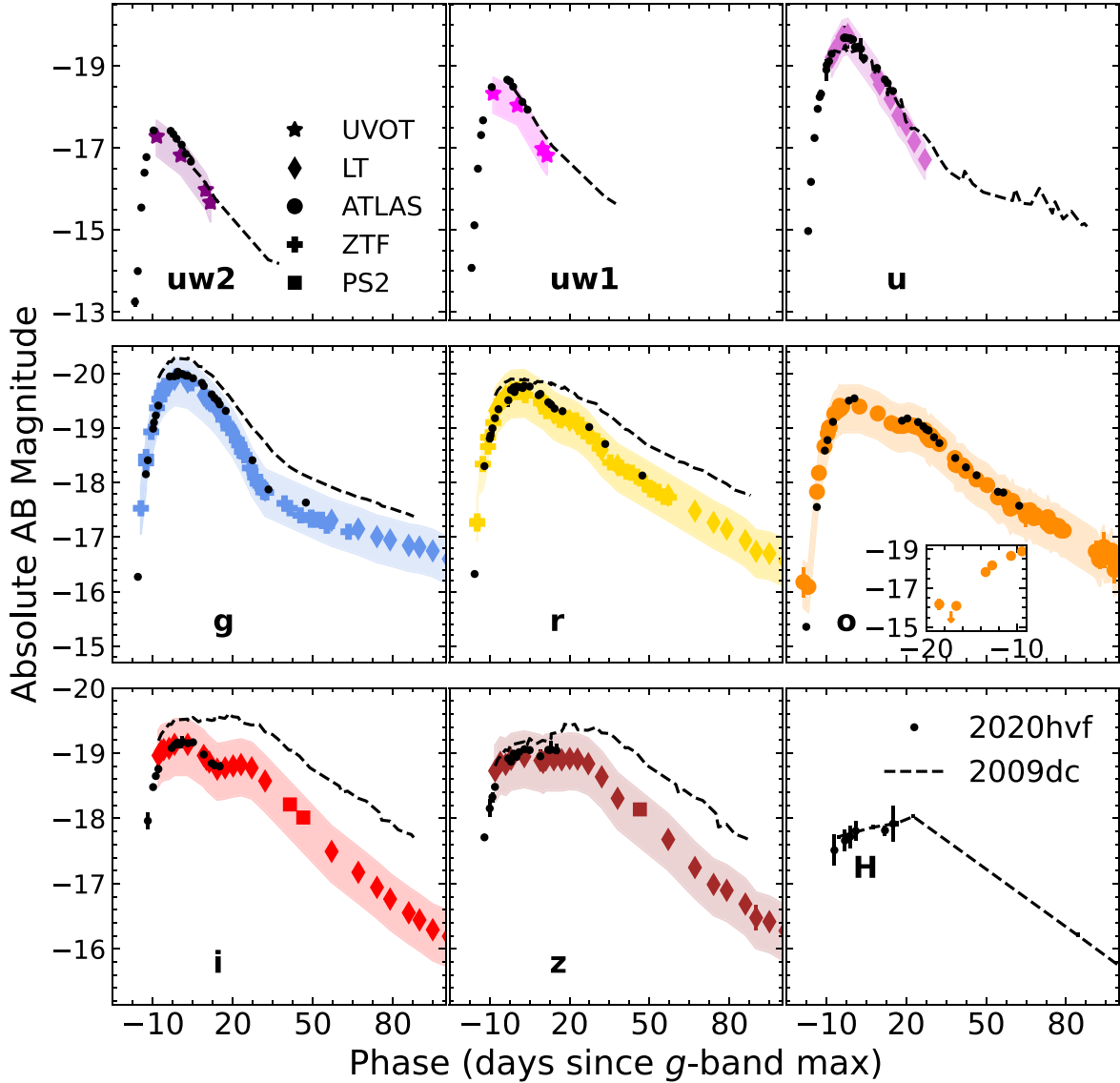
Figure 2. Multiband light-curve evolution of SN 2022ilv (colored symbols), compared to SN 2020hvf (this work) and the luminous SN 2009dc (Silverman et al. 2011; Taubenberger et al. 2011). The absolute magnitudes for SN 2022ilv were computed for the assumed distance of 114 Mpc (corresponding to $z = 0.026$). The shaded regions represent the range of absolute magnitudes for a distance range of 91–136 Mpc. Inset for the o-band light curve (middle right panel) shows the early excess detected by ATLAS. All magnitudes are in the AB system.

59690.52. A clear 5σ detection is recovered on the following day MJD 59691.26, with SN 2022ilv subsequently showing the usual SN-like rise. The detection on MJD 59689.38 and the subsequent non-detection on MJD 59690.52 indicates a short-lived early excess in the light curve of SN 2022ilv. The timescale of this excess is similar to that of SN 2020hvf (Jiang et al. 2021). Although we do not have as high-cadence observations for SN 2022ilv as those for SN 2020hvf, we do have an extra ATLAS observation that further constrains the sharp SN 2020hvf rise shown by Jiang et al. (2021).

3.2. Multiband Light Curves

The multiband light-curve evolution of SN 2022ilv is shown in Figure 2. Also shown are the light curves of SN 2020hvf (this work) and SN 2009dc (Silverman et al. 2011; Tauben-berger et al. 2011). The observed magnitudes of SN 2022ilv and SN 2020hvf were corrected for foreground Galactic extinction (Schlafly & Finkbeiner 2011), with $R_V = 3.1$ and E($B - V$) = 0.11 and 0.04, respectively. The *UBVRI* magnitudes of SN 2009dc were converted to *ugriz* using the transformations prescribed by Jester et al. (2005). For a meaningful comparison, we convert the extinction-corrected apparent magnitudes to absolute magnitudes, assuming $\mu = 35.28^{+0.39}_{-0.47}$ for SN 2022ilv (Section 2.2). The shaded region in the plot shows the range of absolute magnitudes for the range in distance (91–136 Mpc) for SN 2022ilv.

The large uncertainty in the distance translates to a large uncertainty in the peak absolute magnitude for SN 2022ilv, with $M_g^{\text{peak}} = -19.89^{-0.39}_{+0.47}$. Even at the lower distance limit of 91 Mpc, the peak luminosity of SN 2022ilv is $M_g^{\text{peak}} \gtrsim -19.4$, comparable to or more luminous than that of normal SNe Ia. The g-band decline rates for SN 2022ilv and SN 2020hvf are identical, $\Delta m_{15}(g) = 0.58 \pm 0.05$. The derived g-band decline rate for SN 2009dc is also similar within uncertainties, $\Delta m_{15}(g) \approx 0.56 \pm 0.04$. SN 2009dc was very luminous, with a derived $M_g^{\text{peak}} \approx -20.3$.
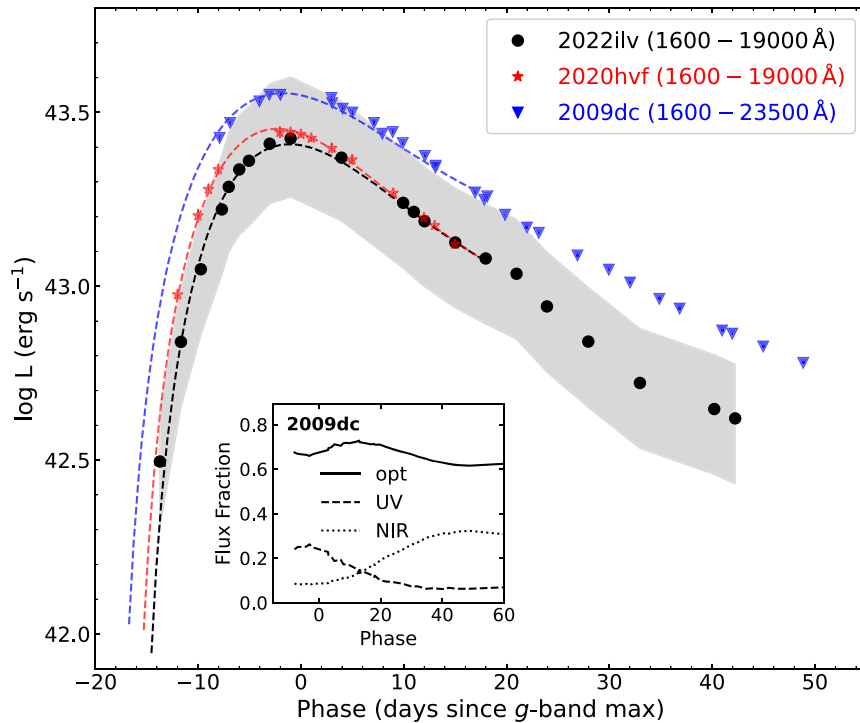
Figure 3. Bolometric light curves of SN 2022ilv (1600–23500 Å), SN 2020hvf (1600–19000 Å), and SN 2009dc (1600–23500 Å). The shaded region represents the luminosity range for SN 2022ilv given the uncertainty in the distance. Inset shows the fractional flux contribution from optical, UV, and NIR bands to the total bolometric flux of SN 2009dc. Dashed lines represent the best-fitting Arnett models for each SN.

3.3. Bolometric Light Curves

The quasi-bolometric light curves of SN 2022ilv and SN 2020hvf were computed from the broadband optical *ugcroiz* magnitudes using the `SuperBol` code (Nicholl [2018]). The UV-optical-NIR bolometric light curve of SN 2009dc was computed from the published photometry using the same method for consistency. For SN 2020hvf, we also compute a UV-optical-NIR bolometric light curve using the UVOT and LT *H*-band photometry.

Since SN 2022ilv and SN 2009dc show a similar spectral evolution (Figure [4]), we compute the time-dependent fractional UV ($uvw2 - m2 - w1$) and NIR (JHK) contribution to the bolometric flux for SN 2009dc and apply those corrections to compute a UV-optical-NIR bolometric light curve for SN 2022ilv assuming a similar fractional contribution in the UV and NIR. The bolometric light curves of SN 2022ilv (1600–23500 Å), SN 2020hvf (1600–19000 Å), and SN 2009dc (1600–23500 Å) are shown in Figure [3]. The shaded region represents the range of luminosity for SN 2022ilv for the distance range. The inset shows the time-dependent fractional flux contribution from the optical ($UBVRI$), UV ($uvw2 - m2 - w1$), and NIR (JHK) to the bolometric light curve of SN 2009dc. We use the Arnett model (Arnett [1982]; Valenti et al. [2008]) to estimate explosion parameters from the bolometric light curves. We fit for ^{56}Ni mass M_{Ni}, ejected mass M_{ej}, kinetic energy E_k, and rise time t_r and fix the opacity at $\kappa = 0.1$ cm^2 g^{-1}. The photospheric velocity v_{ph} from the Si II $\lambda6355$ velocity around maximum for each SN was measured to constrain the fits. For SN 2022ilv, we measure $9000 < v_{ph} < 12{,}000$ km s^{-1}, depending on the adopted red-shift, leading to explosion parameters in the ranges $M_{Ni} \sim 0.7$–$1.5\ M_{\odot}$, $M_{ej} \sim 1.6$–$2.3\ M_{\odot}$, and $E_{51} \sim 0.8$–2.0 foe.

3.4. Spectral Features

The spectra of SN 2022ilv are almost identical to the luminous, carbon-rich SN 2009dc (Figure [4]) for an adopted redshift of $z = 0.021$. SN 2022ilv shows a prominent C II $\lambda6580$ feature in the -8.9 day spectrum that is comparable in strength to the Si II $\lambda6355$ feature, with C II $\lambda7234$ also detected. This C II feature persists until well beyond maximum and is clearly detected in the $+9.1$ day spectrum for SN 2022ilv, as in the case of other 2003fg-like events. For the mean adopted redshift of $z = 0.026 \pm 0.005$ for SN 2022ilv, we deduce a Si II $\lambda6355$ velocity of $\sim11{,}500$ km s^{-1} at -8.9 days, slowing down to $\sim10{,}200$ km s^{-1} at $+4.0$ days, with a systematic uncertainty of 1500 km s^{-1} owing to the uncertainty in redshift.

The C II $\lambda6580$ feature is also detected in the -8.9 day spectrum of SN 2020hvf. It is weaker than the other two and does not persist beyond the epoch of maximum. SN 2020hvf shows very high expansion velocities, particularly in the pre-maximum phase. The broadened and asymmetric Si II $\lambda6355$ line profile in SN 2020hvf likely has a contribution from a high-velocity ejecta component. Using a Gaussian fit, we deduce a Si II expansion velocity of 20300 ± 700 km s^{-1} at -16.9 days, falling to 12800 ± 600 km s^{-1} by $+1.1$ days. Broad O I $\lambda7774$ is also detected in the -16.9 days spectrum at a comparable velocity of 20200 ± 800 km s^{-1}.

4. Analysis of the Early Flux Excess

An early flux excess was detected in high-cadence ATLAS observations of the field of SN 2022ilv (Section [3.1]), the timescale (~1 day) of which is comparable to that detected in SN 2020hvf (Jiang et al. [2021]). ATLAS also caught SN 2020hvf during the early excess phase (Figure [5]); however, the 2 day cadence at the time meant that positive identification
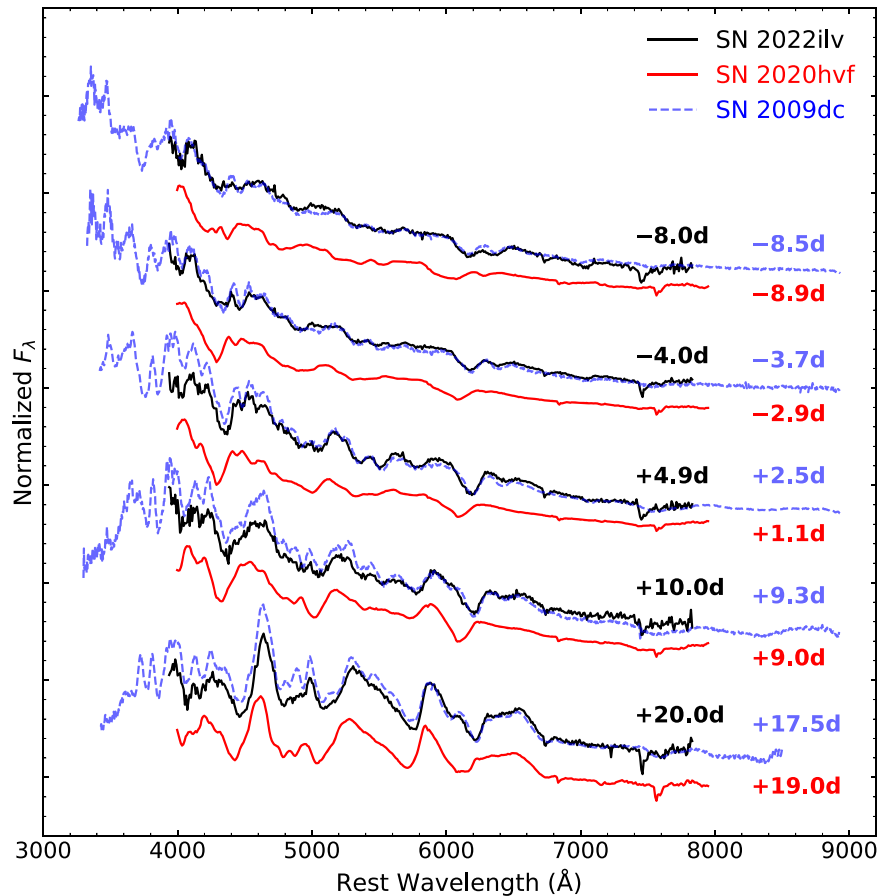
Figure 4. Our LT spectra (with SPRAT) of SN 2022ilv and SN 2020hvf (this work), plotted with the spectra of SN 2009dc (Taubenberger et al. 2011) at similar epochs for comparison. The spectra of SN 2022ilv and SN 2020hvf will be made available on the Weizmann Interactive Supernova Data Repository (WISeREP; Yaron & Gal-Yam 2012).

of this feature was not possible. The most promising scenario to explain this pulse-like, short-lived early excess involves the interaction of fast-moving SN ejecta with dense, confined CSM (e.g., Piro & Morozova 2016; Jiang et al. 2018). The CSM is shock-heated and subsequently cools, powering this initial peak (Piro 2015). Following the one-zone analytic formulation of Piro (2015) for the interaction-powered emission, the timescale of the excess depends on the amount of extended CSM as

$$t_{\mathrm{p}} \approx \left(\frac{M_{\mathrm{e}} \kappa}{v_{\mathrm{e}} c} \right)^{1/2}. \tag{2}$$

Here, M_{e} is the mass of the extended CSM, κ is the electron-scattering opacity of the material, and v_{e} is the velocity of the shocked CSM. The fraction of kinetic energy from the ejecta that is deposited into the CSM (E_{e}) depends on the SN ejecta mass (M_{ej}) and kinetic energy (E_{51}) as

$$E_{\mathrm{e}} \approx 4 \times 10^{49} E_{51} \left(\frac{M_{\mathrm{ej}}}{M_{\odot}} \right)^{-0.7} \left(\frac{M_{\mathrm{e}}}{0.01 \, M_{\odot}} \right)^{0.7}. \tag{3}$$

The peak luminosity for the emission is given by

$$L_{\mathrm{p}} \approx \frac{E_{\mathrm{e}} R_{\mathrm{e}}}{v_{\mathrm{e}} t_{\mathrm{p}}^2}. \tag{4}$$

Here, R_{e} is the initial extent or inner radius of the extended CSM. The radius of the extended material as a function of time is $R(t) = R_{\mathrm{e}} + v_{\mathrm{e}} t$. The time-dependent interaction-powered

luminosity is thus denoted as

$$L(t) = \frac{t_{\mathrm{e}} E_{\mathrm{e}}}{t_{\mathrm{p}}^2} \exp \left[-\frac{t(t + 2t_{\mathrm{e}})}{2t_{\mathrm{p}}^2} \right], \tag{5}$$

where t_{e} is the characteristic expansion timescale, $t_{\mathrm{e}} = R_{\mathrm{e}}/v_{\mathrm{e}}$. We note that the model is quite degenerate, and the interaction-powered luminosity (Equation (5)) is sensitive to the choice of several parameters such as M_{e}, κ, and E_{51}, which in turn depends on ejecta mass M_{ej} and the bulk photospheric velocity for the ejecta, v_{ph}. Equation (2) suggests that the timescale of the emission depends primarily on the CSM mass M_{e}. The duration of the pulse therefore provides an important constraint on the amount of extended material around the WD progenitor. The peak luminosity of the pulse, on the other hand, depends mainly on the radial extent of the CSM rather than its mass (Equation (4)).

Using the constraints from modeling the bolometric light curve of SN 2022ilv (Section 3.3), we fix $M_{\mathrm{ej}} \sim 2 \, M_{\odot}$ and $v_{\mathrm{ph}} \sim 10,000 \, \mathrm{km \, s^{-1}}$. Given the degeneracy in the model and the uncertainty on distance, we expect these parameters to be uncertain by a factor of $\sim$2. The electron-scattering opacity was set at $\kappa = 0.2 \, \mathrm{cm^2 \, g^{-1}}$ assuming hydrogen-poor CSM (Piro 2015). For extended material present at a distance of $R_e \sim 10^{13}$ cm, the resulting ejecta–CSM interaction and subsequent shock-cooling is expected to produce a luminous excess mostly in the optical/UV (Raskin & Kasen 2013). The
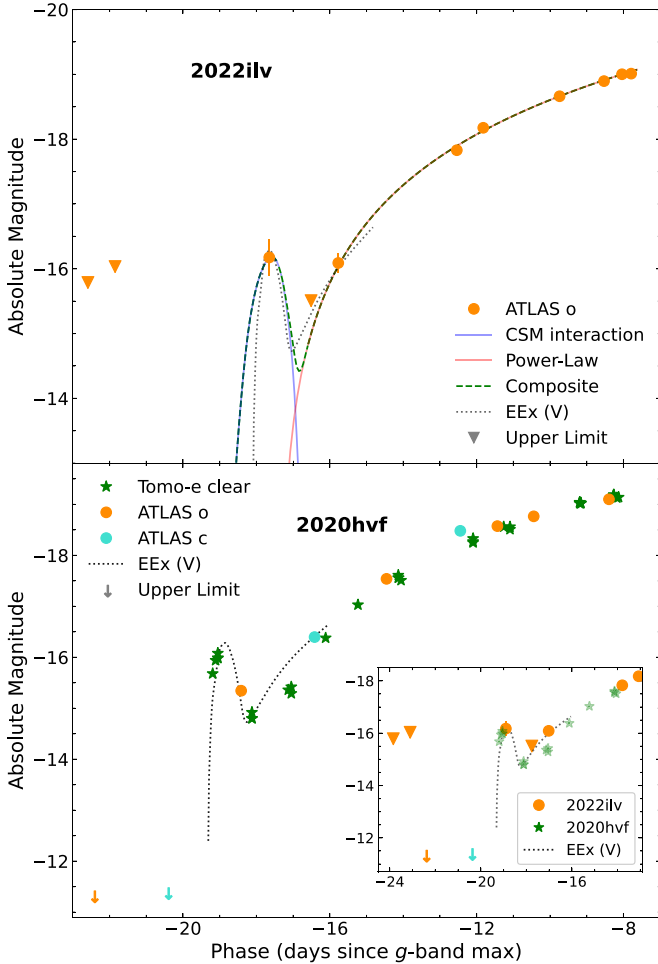
Figure 5. Top panel: ATLAS o-band absolute magnitude light curve of SN 2022ilv, with the synthetic o-band Piro (2015) model for the interaction-powered early excess and a power-law fit to the radioactively driven subsequent rise. The composite model (sum of the two) is shown as a dashed line. A SNEC-based CSM model (EEx) computed by Jiang et al. (2021) to explain the short-lived early excess emission observed in SN 2020hvf is shown for comparison. Bottom panel: the Tomo-e (clear filter) light curve of SN 2020hvf from Jiang et al. (2021), along with our ATLAS photometry that enhances the sampling of the published pulse. Inset: a zoomed-in plot showing a comparison of the early excess feature in SN 2022ilv and SN 2020hvf. Since SN 2020hvf has a longer rise time, the light curve of SN 2022ilv was shifted by ≈1 day to match with SN 2020hvf.

luminosity of the excess emission detected by ATLAS, at $M_o \sim -16.2$ mag, is consistent with CSM present at $R_e \sim 10^{13}$ cm. Finally, the ~ 1 day timescale of the excess emission indicates a small amount of CSM. We find that a CSM mass of $M_e \sim 10^{-3}\ M_\odot$ provides a reasonable fit to the observed excess. Assuming blackbody emission, we estimated a temperature for the shock-heated CSM, and model light curves in different bands were computed from synthetic photometry using synphot (STScI Development Team 2018).

The post-excess, rising o-band light curve of SN 2022ilv was fit with a simple power law (Firth et al. 2015) as

$$F = \alpha(t - t_0)^n. \tag{6}$$

The constant α, time of explosion t_0, and the exponent n were varied as free parameters and the best-fit values are $n = 1.55 \pm 0.18$, $t_0 = 59689.66 \pm 0.69$ (corresponding to -17.8 ± 0.7 rest-frame days relative to the g-band maximum). A composite model for the early light curve was computed by

summing the flux from the ejecta–CSM interaction model of Piro (2015) and the power-law model of the radioactively driven rise (see Figure 5). Also shown is the synthetic V-band light curve computed by Jiang et al. (2021) to explain the observed early excess in SN 2020hvf. The Jiang et al. (2021) model involves a more sophisticated treatment for the density profile of the extended CSM formulated by Piro & Morozova (2016), and synthetic light curves were computed using the SuperNova Explosion Code (SNEC; Morozova et al. 2015).

The Jiang et al. (2021) model for the early excess of SN 2020hvf provides a very reasonable fit, without any scaling in time or luminosity axes, to the early excess and subsequent rise for SN 2022ilv. The timescale of our Piro (2015) model is comparable to that of the Jiang et al. (2021) EEx model. However, we note that Jiang et al. (2021) estimate a CSM mass of $10^{-2}\ M_\odot$, roughly an order of magnitude higher than our estimate based on the simpler analytic approach.

The inset in Figure 5 shows the early excess feature in the two events SN 2022ilv and SN 2020hvf. Although the features are comparable in terms of luminosity and timescale, we are limited in constraining the CSM properties due to the uncertainty in the distance for SN 2022ilv and the cadence of the observations. Although the uncertainty in distance yields large uncertainties on the explosion parameters for SN 2022ilv, the mean $M_{\rm ej}$ of $\sim 2\ M_\odot$ is similar to that inferred for SN 2020hvf. Assuming the CSM opacity κ and timescale t_p of the two events is similar, Equation (2) suggests that the higher photospheric velocity of SN 2020hvf around peak ($\sim 13{,}000$ km s^{-1}, in contrast to $\sim 10{,}000$ km s^{-1} for SN 2022ilv) would imply a higher CSM mass for SN 2020hvf compared to SN 2022ilv by a factor of ~ 1.3. High-cadence, multiband observations of these early excess features in more such Ia-SC events will reveal further insights into the properties of the CSM around their WD progenitors.

5. Discussion and Conclusions

The early excess detected in these two peculiar and luminous SNe Ia (SN 2020hvf and SN 2022ilv) was tentatively also detected in the 2003fg-like events ASASSN-15pz (Chen et al. 2019) and LSQ12gpw (Jiang et al. 2018). This feature could be common within the family of carbon-rich, luminous SNe Ia. The short timescale of the excess, low intrinsic volumetric rate of these events, and limitations in cadence and sensitivity of surveys are factors that may have curtailed previous discoveries. Rapid real-time detection and follow-up of this early excess feature in more such events will enhance our understanding of the nature of the progenitor.

A lingering question for 2003fg-like events is whether the high luminosities of the main peaks are purely radioactively driven, or if interaction with surrounding material boosts the (otherwise normal) luminosity. Super-$M_{\rm Ch}$ WD progenitors have been invoked for many 2003fg-like events (Taubenberger 2017) to explain their extreme properties. Such super-$M_{\rm Ch}$ models succeed in reproducing the high luminosity and broad light-curve shape. Double WD merger simulations show that tidal stripping of the secondary can eject $\sim 10^{-4}$–$10^{-2}\ M_\odot$ of material (Raskin & Kasen 2013; Dan et al. 2014), forming a carbon/oxygen-rich CSM. If the time lag between merger and explosion is a few hours ($\sim 10^4$ s), the CSM would be placed at $\sim 10^{13}$ cm from the WD (Raskin & Kasen 2013), consistent with our estimates from modeling the early excess for SN 2022ilv (Section 4). However, the super-$M_{\rm Ch}$ scenario has

some shortcomings. Nebular spectra of SN 2009dc and SN 2012dn (among other 2003fg-like SNe) show clear evidence of a low ionization state (Taubenberger et al. 2013, 2019), contrary to what is expected for a large amount of heating from a high ^{56}Ni mass.

A plausible alternative to the super-M_{Ch} scenario is a normal M_{Ch} explosion occurring within a dense, carbon and oxygen-rich envelope (e.g., Hachinger et al. 2012; Taubenberger et al. 2013; Noebauer et al. 2016). The empirical correlation between the Si II velocity and strength of the C II feature in a sample of 2003fg-like events (Ashall et al. 2021) supports this idea. It may explain the prominent and persistent C II features observed owing to a large amount of unburnt material. SN 2020esm (Dimitriadis et al. 2022) shows premaximum spectra almost entirely dominated by unburnt carbon and oxygen. The interaction of SN ejecta with the surrounding material provides enhanced luminosity, and the reverse shock would decelerate the ejecta (Noebauer et al. 2016), potentially explaining the combination of high luminosity and low velocity. Noebauer et al. (2016) estimated a carbon/oxygen-rich CSM mass of $\sim$0.6 $M_\odot$ for SN 2009dc through detailed hydrodynamic simulations. While their models reproduced the light-curve shape of SN 2009dc remarkably well, it had too low a luminosity by a factor of 0.2 dex. The early excess observed in SN 2022ilv requires $M_e \sim 10^{-3}$ $M_\odot$ within a radius $R_e \sim 10^{13}$ cm, implying a density of order $\sim 10^{-11}$ g cm^{-3}. The Noebauer et al. (2016) model requires a much larger mass of $\sim$0.6 $M_\odot$ with a power-law density profile between $\sim 10^{-9}$ g cm^{-3} and $\sim 10^{-10}$ g cm^{-3} out to $R_e \sim 1.4 \times 10^{14}$ cm. If CSM contributes to both the early excess and the main luminosity peak, it would likely require two separate components or a structured CSM profile.

If such a significant amount of carbon/oxygen-rich CSM is the explanation for either the pulse or main peak, then its origin remains mysterious. This could be a natural outcome of the double-degenerate scenario, wherein the disruption and sub-sequent accretion of the secondary WD lead to the formation of a hot, spherical CO envelope and a centrifugally supported disk (Yoon et al. 2007). Simulations have shown that the outcome is sensitive to whether the explosion occurs promptly after the merger (Moll et al. 2014), or after a lag (Raskin et al. 2014). Hsiao et al. (2020) and Ashall et al. (2021) have suggested an alternative of a CO WD merging with the degenerate core of an asymptotic giant branch star, or the core-degenerate scenario (Kashi & Soker 2011). This scenario predicts a significant X-ray luminosity due to the interaction, which should be detectable in nearby events. The lack of narrow emission features in observed spectra of 2003fg-like events is a significant shortcoming of all interaction-based scenarios. Photometric, spectroscopic, and polarimetric observations of more such events, in conjunction with modeling efforts and binary population synthesis calculations, will be necessary for unraveling the progenitor puzzle.

The luminous family of 2003fg-like SNe Ia is known to occur preferentially either in low-luminosity hosts or remote locations in luminous hosts (Taubenberger 2017). The limit of $M_r \gtrsim -11$ for the host of SN 2022ilv (Section 2.1) is consistent with these findings. The luminous lenticular galaxy NGC 5872 ($z = 0.024556$; Van den Bosch et al. 2015) is at the right redshift and is offset by $7\farcs7$ from the location of SN 2022ilv or a projected radial separation of $\sim$250 kpc. This could imply the host is a dwarf galaxy satellite of this more luminous and massive galaxy. The striking preference for environments that are likely low-metallicity should be considered for progenitor modeling and scenarios.

ORCID iDs

Shubham Srivastav ● https://orcid.org/0000-0003-4524-6883
S. J. Smartt ● https://orcid.org/0000-0002-8229-1731
M. E. Huber ● https://orcid.org/0000-0003-1059-9603
G. Dimitriadis ● https://orcid.org/0000-0001-9494-179X
K. C. Chambers ● https://orcid.org/0000-0001-6965-7789
Michael D. Fulton ● https://orcid.org/0000-0003-1916-0664
Thomas Moore ● https://orcid.org/0000-0001-8385-3727
F. P. Callan ● https://orcid.org/0000-0002-7975-8185
James H. Gillanders ● https://orcid.org/0000-0002-8094-6108
K. Maguire ● https://orcid.org/0000-0002-9770-3508
M. Nicholl ● https://orcid.org/0000-0002-2555-3192
Luke J. Shingles ● https://orcid.org/0000-0002-5738-1612
S. A. Sim ● https://orcid.org/0000-0002-9774-1192
K. W. Smith ● https://orcid.org/0000-0001-9535-3199
J. P. Anderson ● https://orcid.org/0000-0003-0227-3451
Thomas de Boer ● https://orcid.org/0000-0001-5486-2747
Ting-Wan Chen ● https://orcid.org/0000-0002-1066-6098
Hua Gao ● https://orcid.org/0000-0003-1015-5367
D. R. Young ● https://orcid.org/0000-0002-1229-2499

References

Arnett, W. D. 1982, ApJ, 253, 785
Ashall, C., Lu, J., Hsiao, E. Y., et al. 2021, ApJ, 922, 205
Astropy Collaboration, Price-Whelan, A. M., Lim, P. L., et al. 2022, ApJ, 935, 167
Bellm, E. C., Kulkarni, S. R., Graham, M. J., et al. 2019, PASP, 131, 018002
Blondin, S., & Tonry, J. L. 2007, ApJ, 666, 1024
Brown, P. J., Holland, S. T., Immler, S., et al. 2009, AJ, 137, 4517
Burke, J., Howell, D. A., McCully, C., et al. 2022, TNSCR, 2022-1137, 1
Chambers, K. C., Magnier, E. A., Metcalfe, N., et al. 2016, arXiv:1612.05560
Chen, P., Dong, S., Katz, B., et al. 2019, ApJ, 880, 35
Dan, M., Rosswog, S., Brüggen, M., & Podsiadlowski, P. 2014, MNRAS, 438, 14
Deckers, M., Maguire, K., Magee, M. R., et al. 2022, MNRAS, 512, 1317
Dey, A., Schlegel, D. J., Lang, D., et al. 2019, AJ, 157, 168
Dimitriadis, G., Foley, R. J., Arendse, N., et al. 2022, ApJ, 927, 78
Firth, R. E., Sullivan, M., Gal-Yam, A., et al. 2015, MNRAS, 446, 3895

Gehrels, N., Chincarini, G., Giommi, P., et al. 2004, ApJ, 611, 1005
Hachinger, S., Mazzali, P. A., Taubenberger, S., et al. 2012, MNRAS, 427, 2057
Hicken, M., Garnavich, P. M., Prieto, J. L., et al. 2007, ApJL, 669, L17
Howell, D. A., Sullivan, M., Nugent, P. E., et al. 2006, Natur, 443, 308
Hsiao, E. Y., Hoeflich, P., Ashall, C., et al. 2020, ApJ, 900, 140
Jester, S., Schneider, D. P., Richards, G. T., et al. 2005, AJ, 130, 873
Jiang, J.-a., Doi, M., Maeda, K., & Shigeyama, T. 2018, ApJ, 865, 149
Jiang, J.-a., Maeda, K., Kawabata, M., et al. 2021, ApJL, 923, L8
Kasen, D. 2010, ApJ, 708, 1025
Kashi, A., & Soker, N. 2011, MNRAS, 417, 1466
Levanon, N., & Soker, N. 2017, MNRAS, 470, 2510
Lu, J., Ashall, C., Hsiao, E. Y., et al. 2021, ApJ, 920, 107
Magee, M. R., Maguire, K., Kotak, R., et al. 2020, A&A, 634, A37
Magnier, E. A., Chambers, K. C., Flewelling, H. A., et al. 2020, ApJS, 251, 3
Maoz, D., Mannucci, F., & Nelemans, G. 2014, ARA&A, 52, 107
Moll, R., Raskin, C., Kasen, D., & Woosley, S. E. 2014, ApJ, 785, 105
Morozova, V., Piro, A. L., Renzo, M., et al. 2015, ApJ, 814, 63
Nicholl, M. 2018, RNAAS, 2, 230
Noebauer, U. M., Taubenberger, S., Blinnikov, S., Sorokina, E., & Hillebrandt, W. 2016, MNRAS, 463, 2972
Piro, A. L. 2015, ApJL, 808, L51
Piro, A. L., & Morozova, V. S. 2016, ApJ, 826, 96
Polin, A., Nugent, P., & Kasen, D. 2019, ApJ, 873, 84

Raskin, C., & Kasen, D. 2013, ApJ, 772, 1
Raskin, C., Kasen, D., Moll, R., Schwab, J., & Woosley, S. 2014, ApJ, 788, 75
Roming, P. W. A., Kennedy, T. E., Mason, K. O., et al. 2005, SSRv, 120, 95
Scalzo, R. A., Aldering, G., Antilogus, P., et al. 2010, ApJ, 713, 1073
Schlafly, E. F., & Finkbeiner, D. P. 2011, ApJ, 737, 103
Shappee, B. J., Holoien, T. W. S., Drout, M. R., et al. 2019, ApJ, 870, 13
Silverman, J. M., Ganeshalingam, M., Li, W., et al. 2011, MNRAS, 410, 585
Smith, K. W., Smartt, S. J., Young, D. R., et al. 2020, PASP, 132, 085002
Smith, K. W., Williams, R. D., Young, D. R., et al. 2019, RNAAS, 3, 26
Steele, I. A., Smith, R. J., Rees, P. C., et al. 2004, Proc. SPIE, 5489, 679
STScI Development Team 2018, synphot: Synthetic Photometry using Astropy, Astrophysics Source Code Library, ascl:1811.001
Taubenberger, S. 2017, in Handbook of Supernovae, ed. A. W. Alsabti & P. Murdin (Berlin: Springer), 317
Taubenberger, S., Benetti, S., Childress, M., et al. 2011, MNRAS, 412, 2735
Taubenberger, S., Floers, A., Vogl, C., et al. 2019, MNRAS, 488, 5473
Taubenberger, S., Kromer, M., Hachinger, S., et al. 2013, MNRAS, 432, 3117
Tonry, J. L., Denneau, L., Flewelling, H., et al. 2018a, ApJ, 867, 105
Tonry, J. L., Denneau, L., Heinze, A. N., et al. 2018b, PASP, 130, 064505
Valenti, S., Benetti, S., Cappellaro, E., et al. 2008, MNRAS, 383, 1485
Van den Bosch, R. C. E., Gebhardt, K., Gültekin, K., Yıldırım, A., & Walsh, J. L. 2015, ApJS, 218, 10
Yaron, O., & Gal-Yam, A. 2012, PASP, 124, 668
Yoon, S. C., Podsiadlowski, P., & Rosswog, S. 2007, MNRAS, 380, 933